CMES

Computer Modeling in Engineering & Sciences

Founder and Editor-in-Chief:
Satya N. Atluri
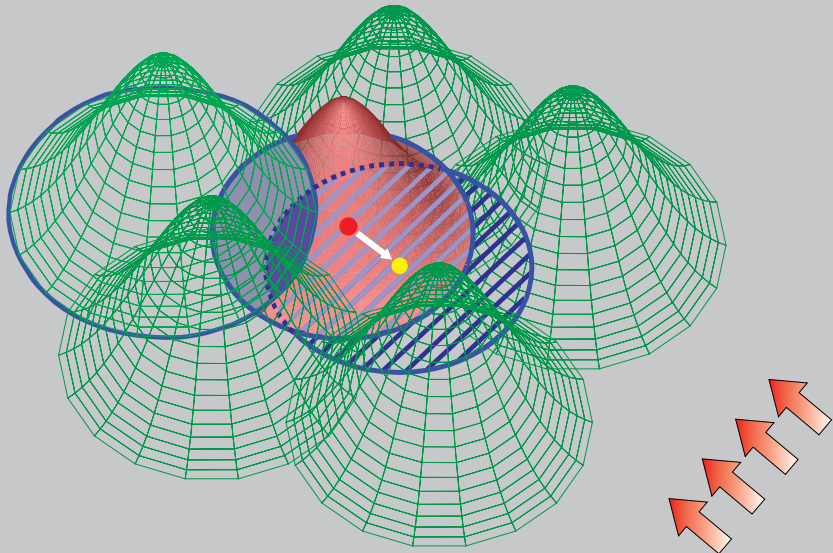
Recent Developments on Thermo-Mechanical Simulations of Ductile Failure by Meshfree Method

B. Ren[1,2]**, J. Qian**[1]**, X. Zeng**[1]**, A. K. Jha**[3]**, S. Xiao**[4] **and S. Li**[1,5]

Abstract: Ductile failure is a complex multi-scale phenomenon evolved from the micro-voids to macro-crack. There are three main failure mechanisms behinds a ductile failure: adiabatic shear band (ASB), spall fracture, and crack. Since this type of thermo-mechanical phenomena involves large deformation and large scale plastic yielding, a meshfree method has intrinsic advantages in solving this kind of problems over the conventional finite element method. In this paper, the numerical methodologies including multi-physics approach for ASB, parametric visibility condition for crack propagation, and multi-scale approach to determine spall strength in simulating ductile failure have been reviewed. A thermo-mechanical coupling algorithm is proposed to incorporate reproducing kernel particle method (RPKM) with rate dependent Johnson-Cook model. Numerical simulations demonstrate that this meshfree method can capture the essential features of a ductile failure.

Keywords: meshfree, thermo-mechanical, ductile failure, adiabatic shear band, crack, spall fracture

1   Introduction

During the past decades, many experiments have revealed that the ductile failure in metal under shock wave due to collision, explosion, etc. leads to extremely high strain rate (up to 10^6 m/s) with large local plastic deformation. This is in contrast

[1] Department of Civil and Environmental Engineering, University of California, Berkeley, CA 94720, USA

[2] School of Hydro-power and Information Engineering, Huazhong University of Science and Technology, Wuhan 430074, China

[3] NextGen Aeronautics, 2780 Skypark Drive, Suite 400, Torrance, CA 90505, USA

[4] Department of Mechanical and Industrial Engineering, The University of Iowa, Iowa City, IA 52242, USA

[5] School of Civil Engineering and Mechanics, Huazhong University of Science and Technology, Wuhan 430074, China. Corresponding Email: shaofan@berkeley.edu

with a brittle failure where cracks are nucleated and evolved with small plastic deformation [Chevrier and Klepaczko (1999)]. The ductile failure can be interpreted as the result of voids nucleation-growth-coalescence effect. At micro-scale (about 0.1 to 10 μm), the voids are nucleated from inhomogeneities and inclusion inside solid driven by the positive hydrostatic stress [Antoun et al. (2003)]. With positive tri-axial stress and shear stress [Nahshon and Hutchinson (2008)], the volume of voids may increase and some neighboring voids could be trigged by localized deformation. Such voids coalescence may lead to material instability at meso-scale (10 to 300 μm) [Chevrier and Klepaczko (1999)]. When voids coalesce to each other, the macro-scale cracks will be formed. During such nucleation-growth-coalescence process, three main failure morphologies: spall fracture, shear band, and cleavage cracking [Chevrier and Klepaczko (1999)] may take place. Here, shear band is a un-cleavage damage phenomenon. Spall fracture is dominated by voids growth and coalescence. And, a crack can be found at macro-scale fracture evolving into separating boundaries inside a solid. Although several studies have been conducted to simulate ductile failure [McVeigh and Liu (2009)], most of these studies deal with the three kinds of material failure mechanisms separately.

There are two types of mesh sensitivities in mesh-based computational method, e.g. FEM. The first type of mesh-dependent sensitivity comes from the rate-independent plasticity. Since the rate-independent theories admit infinitesimal plastic zone near-zero-width singular surface solution, the discrete finite element size cannot capture this weak discontinuous surface accurately. The second type of mesh-dependent sensitivity is the so-called mesh-alignment sensitivity. There are essentially two approaches to simulate the evolving solid separation in FEM mesh topology: (1) embed the possible crack path in the original FEM mesh, which leads to crack propagating along the pre-set crack path, and (2) use 'killing element' and remeshing technology, in which the crack path is limited along element boundaries. Both of the two approaches have obvious limitations to capture the crack path accurately. When a ductile failure is associated with finite plastic deformation, the process becomes irreversible. Mathematically speaking, the element death and remeshing approach is difficult to be implemented for ductile failure because plastic process is history dependent.

Meshfree or particle-based methods have intrinsic advantages to represent the evolving geometry of a solid with crack propagation or fracture. The first well-known particle method is the so-called Smoothed Particle Hydro-Dynamics (SPH), which operates on the strong form of partial differential equations (PDEs) [Li and Liu (2004)]. Another particle method, so-called Meshfree Galerkin method, operates on the Galerkin's weak form of PDEs. In the past decades, several Mesh-free Galerkin methods, such as Diffuse Element Method (DEM), Element Free

Galerkin Method (EFGM), Reproducing Kernel Particle Method (RKPM), H-P Cloud Method, Partition of Unity Method, Meshless Local Petrov-Galerkin Method (MLPG) [Atluri and Zhu (1998); Atluri and Zhu (2000)], have been developed. For contemporary development of meshfree methods, we refer to a review article by Li and Liu [2002]. The applications to simulate adiabatic shear band, spall fracture and crack propagation by RKPM method are reported intensively. In a series of studies, Li and his co-workers have systematically conducted meshfree simulations of ductile failure e.g. [Ren and Li (2010); Li and Liu (2000); Li, Hao, Liu, (2000); Li et al (2001); Li et al (2002)]. In this paper, some recent developments on this topic are reported.

This paper is organized in six sections. In section 2, a thermo-mechanical coupled formula is proposed to incorporate RKPM with Johnson-Cook model. In section 3, 4 and 5, the applications of handling adiabatic shear band, crack propagation and spall fracture are reported, respectively. In section 6, a few remarks and comments are made, and some important issues of ductile fracture have also been discussed there.

2 Thermo-mechanical coupling with meshfree method and Johnson-Cook model

Ductile failure induced by shock wave undergoes enormous plastic deformation, which, in turn, generates a large amount of heat locally. At some locations, temperature can sharply increase up to near melting point [Zhou, Rosakis, Ravichandran (1996a); Zhou, Ravichandran, Rosakis (1996b)]. Hence, to simulate the ductile failure of a solid under shock loading, the thermo-mechanical coupling has to be considered. Using the virtual power principle, the weak form of the linear momentum can be written as:

$$\int_{\Omega_0} \mathbf{P} : \delta \mathbf{F} d\Omega = \int_{\Gamma_0^T} \mathbf{T} \cdot \delta \mathbf{u} dS - \int_{\Omega_0} \rho_0 \frac{\partial^2 \mathbf{u}}{\partial t^2} \cdot \delta \mathbf{u} d\Omega \tag{1}$$

Where $\mathbf{P}$ denotes the nominal stress, which is the transpose of the first Piola–Kirchhoff stress, and it can be related to the Kirchhoff stress as $\tau = \mathbf{P}\mathbf{F}^T$. And, Γ_0^T denotes the traction boundary where the traction force $\mathbf{T}$ is prescribed. Assume that in the domain Ω_0, there is a valid particle distribution of np particles. The displacement field $\mathbf{u}$ can be approximated by the following meshfree interpolation,

$$\mathbf{u}^h(\mathbf{X}, t) = \sum_{I=1}^{np} N_I(\mathbf{X}) \mathbf{U}_I(t) \tag{2}$$

Here, N_I is the meshfree interpolation shape function at a specified particle I. $\mathbf{U}_I$ is the displacement at particle I.

Equation (1) yields the following discrete equations [Ren and Li (2010)]:

$$\mathbf{M}\frac{\partial^2 \mathbf{u}}{\partial t^2} = \mathbf{f}^{ext} - \mathbf{f}^{int} \tag{3}$$

where M is the mass matrix that may be lumped by the row-sum; the external force vector $\mathbf{f}^{ext}$ and internal force vector $\mathbf{f}^{int}$ are given respectively as,

$$\mathbf{f}_I^{ext} = \int_{\Gamma_x} T_i(\mathbf{X},t) N_I \mathbf{e}_i dS \tag{4}$$

$$\mathbf{f}_I^{int} = \int_{\Gamma_x} P_{Ji}^h \frac{\partial N_I}{\partial X_J} \mathbf{e}_i d\Omega, \tag{5}$$

where the Einstein summation convention is applied in Eq.(4) and Eq.(5) for both index i and J.

The interpolation shape function of RKPM may be viewed as an enhanced version of the original SPH shape function as [Li and Liu (2004)]:

$$N_I(\mathbf{X}) = \mathbf{C}(\mathbf{X},\bar{\mathbf{X}})w(\mathbf{X}-\bar{\mathbf{X}})\Delta V_I \tag{6}$$

where $\bar{\mathbf{X}}$ denotes a specific particle, $w(\mathbf{X}-\bar{\mathbf{X}})$ is the kernel function , $\mathbf{C}(\mathbf{X},\bar{\mathbf{X}})$ is the correction function and ΔV_I is the integration volume for particle located at $\bar{\mathbf{X}}$.

Considering the heat generation and conduction process, the strong form of energy balance can be shown as:

$$\rho_0 C_p \frac{\partial T}{\partial t} = \chi \tau : \mathbf{d}^p + \nabla_X \left(J\mathbf{F} \cdot \mathbf{K} \cdot \mathbf{F}^{-T} \cdot \nabla_X T \right) \quad \forall \mathbf{X} \in \Omega \tag{7}$$

where $\mathbf{F}$ is the deformation gradient, T is the temperature, χ^τ denotes the fraction of plastic work converting to heat, ∇ is the gradient operator in the reference configuration, C_p is the specific heat and $\mathbf{d}^p$ is the plastic rate of deformation. For isotropic heat conduction, the heat conductivity tensor will be $\mathbf{K} = \kappa \mathbf{I}$, where κ is the conductivity coefficient.

To build a stable integration algorithm for thermo-mechanical coupling, the operator splitting technique proposed by Armero and Simo [Armero and Simo (1993)] is employed. The energy balance formula including heat generation and conduction is given as:

$$\int_\Omega \rho_0 C_p \frac{\partial T}{\partial t} \delta T d\Omega = \int_\Omega \left(\chi \bar{\tau} \dot{\bar{\varepsilon}} - \left(\mathbf{F}^{-1} \dot{\mathbf{K}} \cdot \mathbf{F}^{-T} \nabla T \right) \right) \delta T d\Omega \tag{8}$$

Subsequently, the discrete weak form can be assembled in the following algebraic equations [Ren and Li (2010)],

$$\mathbf{C} \cdot \dot{\mathbf{T}} = \mathbf{G} - \mathbf{H} \cdot \mathbf{T} \tag{9}$$

where $\mathbf{C}$ is defined as the thermal mass, $\mathbf{G}$ is the matrix related to heat generation due to plastic strain, and $\mathbf{H}$ is the matrix related to heat conductivity.

$$\mathbf{C} = [C_{IJ}], \; C_{IJ} := \int_{\Omega_x} \rho_0 C_p N_I(\mathbf{X}) N_J(\mathbf{X}) \, d\Omega_X \tag{10}$$

$$\mathbf{G} = [G_I], \; G_I := \int_{\Omega_x} \chi \bar{\tau} \dot{\bar{\varepsilon}} N_I(\mathbf{X}) \, d\Omega_X \tag{11}$$

$$\mathbf{H} = [H_{ij}], \; H_{ij} := \int_{\Omega_x} \kappa F_{I\ell}^{-1}(\mathbf{X}) F_{\ell J}^{-T}(\mathbf{X}) N_{i,J}(\mathbf{X}) N_{j,I}(\mathbf{X}) \, d\Omega_X \tag{12}$$

The total rate of deformation of a thermo-mechanical coupling process can be decomposed into three distinct parts, i.e. elastic, plastic and thermal parts as follows,

$$\mathbf{d} = \mathbf{d}^e + \mathbf{d}^p + \mathbf{d}^T \tag{13}$$

A rate form constitutive equation is then formulated,

$$\overset{\nabla}{\tau} = \mathbf{C} : \mathbf{d}^e = \mathbf{C} : \left(\mathbf{d} - \mathbf{d}^p - \mathbf{d}^T \right) \tag{14}$$

where

$$\mathbf{d}^p = \dot{\bar{\varepsilon}} \, \hat{\mathbf{n}} \tag{15}$$

$$\mathbf{d}^T = \alpha \dot{T} \, \mathbf{I} \tag{16}$$

$\hat{\mathbf{n}}$ is the normal of deviatoric stress(s) and:

$$\hat{\mathbf{n}} = \frac{3}{2\bar{\tau}} \mathbf{s} \tag{17}$$

The Johnson-Cook constitutive model [Johnson and Cook (1985)] is adopted to calculate the plastic strain rate $\dot{\bar{\varepsilon}}$:

$$\dot{\bar{\varepsilon}} = \dot{\varepsilon}_0 \exp \left\{ \frac{1}{C} \left(\frac{\sigma_Y}{g(\bar{\varepsilon}, T)} - 1 \right) \right\}. \tag{18}$$

$$g(\bar{\varepsilon}, T) = \left[A + B_\varepsilon^{-n} \right] \left[1 - T^m \right] \tag{19}$$

with $T = \frac{T - T_{room}}{T_{melt} - T_{room}}$.

where $\dot{\varepsilon}_0$ is referential strain rate, normally taken as $1.0 s^{-1}$, n and m is the strain hardening and thermal softening parameters, T_{room} is the room temperature, and T_{melt} is the melting temperature. In Ren and Li (2010), formulas are provided to update stress status in explicit dynamical simulation.

3   Meshfree simulation of adiabatic shear band

3.1   Overview

Shear band is a narrow region of un-cleavage localized shear deformation. It can happen under different loading conditions in various materials [Bai and Dodd (1992)]. When metal and alloy deforms under high strain rate loading e.g. high speed impact or explosion, a specific shear band, also known as adiabatic shear band (ASB), forms. The plastic deformation will generate large amount of heat inside shear band. Comparing with the time scale (normally at several microseconds), most of the heat stays within shear band (hence considered adiabatic), and leads to stress collapse. However, due to the extremely high temperature gradient near the shear band, the heat conduction still plays a crucial role in ASB failure. The shear band phenomena have been observed for more than two decades. Zhou et al [Zhou et al (1996ab)] used a single notch specimen to test the dynamic shear band propagation under various impact speeds. Kalthoff [Kalthoff (1988)] used a double-notch impact specimen to study two shear bands. Li and Liu [Li and Liu (2000)] used meshfree method to simulate strain localization problem and compared with FEM results. Li et al [Li et al (2000)] discussed the abilities of meshfree method to alleviate the mesh-alignment sensitivity associated with strain localization problem such as ASB. Li et al. [Li et al (2001); Li et al (2002)] simulated the failure mode switching (ductile-to-brittle: shear band to crack) phenomena under different impact speeds, which are reported experimentally. They also reported the dynamical shear band propagating along a curved path and high strain rate region in front of shear band tip.

3.2   Criteria of ASB propagation

When ASB is formed, the material response inside shear band is drastically different from the region away from the shear band. Currently, the most efficient method to simulate shear band is to employ normal metal constitutive model in the region away from shear band and soft constitutive model to simulate the plastic flow inside shear band. To implement this model, a crucial step is to set failure criteria for ASB propagation. Several criteria had been proposed e.g. the simple plastic strain and stress criterion by Batra and Kim [Batra and Kim (1992)], dynamic recrystallization criterion by Medyanik et al [Medyanik et al (2007)]. One of the most popular ASB growth criteria is introduced by Zhou et al [Zhou et al (1996b)], which depends on strain rate, and it is given in the following form,

$$\bar{\varepsilon}_{cr} = \varepsilon_1 + (\varepsilon_2 - \varepsilon_1)\frac{\dot{\varepsilon}_r}{\dot{\varepsilon}_r + \dot{\bar{\varepsilon}}} \tag{20}$$

where ε_1, ε_2, $\dot{\varepsilon}_r$ are empirical strain parameters and $\varepsilon_1 < \varepsilon_2$. This criterion suggests

that the critical strain decreases with the growth of strain rate. The critical strain is equal to ε_2 when the strain rate is zero and approaching ε_1 as the strain rate approaches infinity.

3.3 Physical model of ASB

The multi-physics modeling technique is adopted to model the constitutive behaviors for particles inside ASB at different stages. When temperature is high and plastic deformation is dominating, we use a fluid-like model to describe those material particle inside the ASB. In this work, we use a so-called fluid model, which provides the post-localization stress collapse mechanism inside ASB [Zhou et. al. (1996ab)]:

$$\tau = -\frac{\gamma[1 - J + \alpha(T - T_{room})]}{J} \frac{E}{1 - v} \mathbf{I} + \mu \mathbf{d} \tag{21}$$

where τ is Kirchhoff stress tensor, γ is stiffness parameter, μ is a viscosity coefficient, J is the determinate of deformation gradient, and $\mathbf{I}$ is the second order identity tensor.
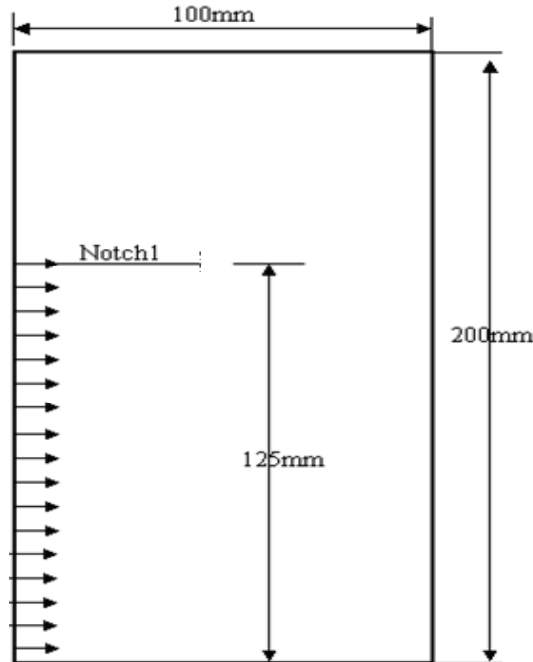
Figure 1: Configuration of ASB experimental specimen.

3.4 Numerical simulations

Zhou et. al. [Zhou, Ravichandran and Rosakis (1996b)] proposed a special ASB experimental set-up, which is now called Zhou-Rosakis-Ravichandran (ZRR) problem. In the experiment, the target plate has a single notch because it can eliminate the interference as well as interaction of the diffracted waves between multi-notches, which occurs in Kalthoff-Winkler (KW) problem [Kalthoff (1988)]. Therefore, a longer and "cleaner" shear band can be observed. The configuration of test is shown as Fig. 1. The Johnson-Cook material constants of the specimen (4340 Steel) and the material constants of the fluid model are listed in Table 1 and Table 2. The parameters in Eq. (18) are shown in Table 3.

With a loading velocity of 40 m/s, the numerical results are shown in Figures 2 to 4. The adiabatic shear band is nucleated about $14\mu s$ after loading. The average velocity of ASB is 1100 m/s and the maximum temperature inside shear band is 1266

Table 1: Johnson-Cook constants of Steel 4340.

Parameter	Value	Definition
E	208 Gpa	Young's modulus
v	0.3	Poisson's ratio
ρ	7830 kgm^{-3}	Mass density
A	792490Mpa	Yield stress
B	510Mpa	Strain Hardening
n	0.26	Strain hardening index
$\dot{\varepsilon}_0$	1.0s^{-1}	Reference strain rate
m	1.03	Temperature softening
C_p	477J(kg.K)$^{-1}$	Specific heat
α	11.2E-06K^{-1}	Coefficient of Thermal expansion
χ	0.9	The fraction of plastic work convert to heat
k	38	Conductivity coefficient

Table 2: Constants of Fluid Model.

Parameter	Value	Parameter	Value	Parameter	Value
γ	0.002	α	3.2d-7	μ	1200

Table 3: Parameters in Criteria of ASB.

Parameter	Value	Parameter	Value	Parameter	Value
ε_1	0.04	ε_2	0.3	$\dot{\varepsilon}_r$	4.0d4

K, which is consistent with the experimental results [Zhou, Rosakis, Ravichandran (1996a)]. In Figure 2, one can find the "curved" shear band path that is very typical in actual ductile failure. The temperature profile of a vertical line located at 4 mm in front of notch tip (Dashed line in Fig. 1, there are 50 points with length of 8 mm) is monitored as shown in Figure 3, which illustrates the heat is generated inside ASB and conducted to surrounding area. Also, the temperature history of one particle inside ASB is shown in Figure 4(a), which describes the heat generation and conduction phenomena. The effective stress-effective strain curve of a particle inside ASB in Figure 4(b) shows the stress collapse inside shear band that has been verified by experiments.
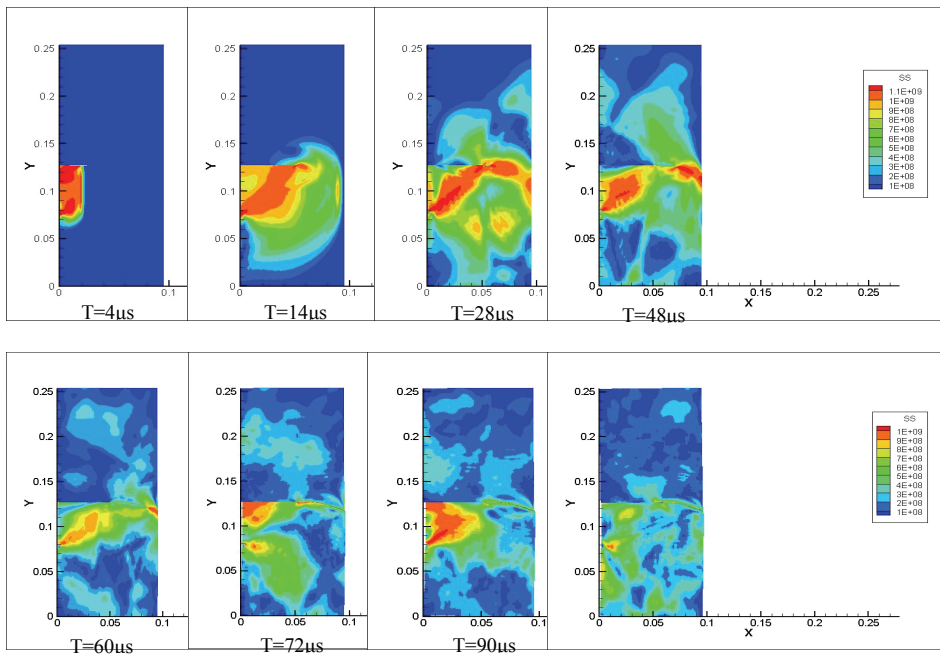
Figure 2: ASB propagation with ductile thermo-mechanical model (effective stress contour).

4 Meshfree simulation of crack propagation

4.1 Overview

Another prominent mode of failure occurring in material under shock loading is the crack propagation. The main challenge in modeling the crack propagation is
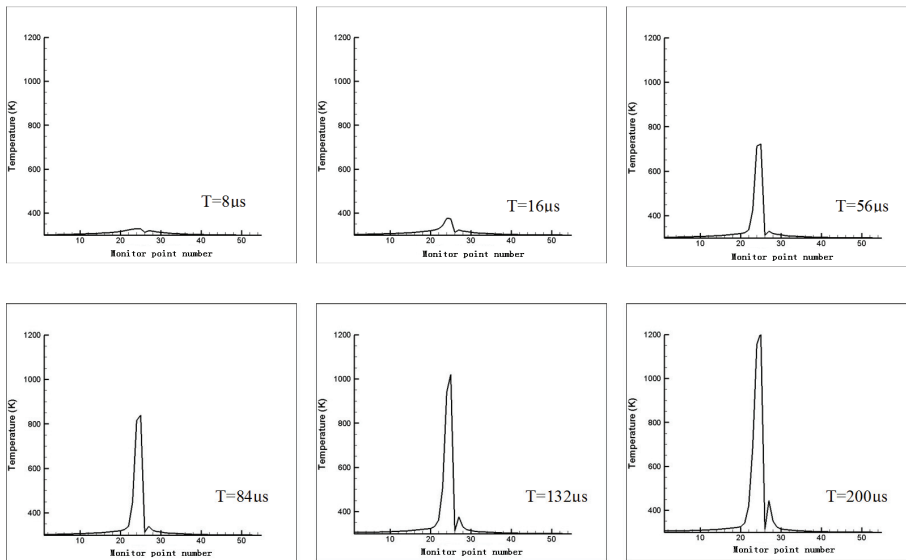
Figure 3: Temperature profile inside ASB.
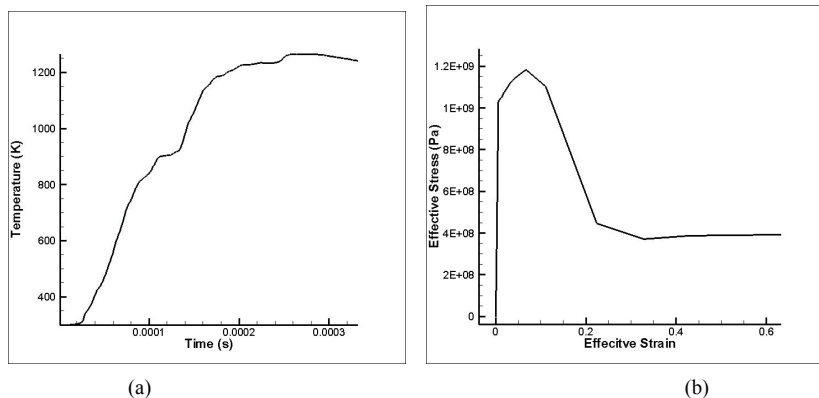
Figure 4: (a) Temperature profile inside ASB, (b) Effective stress, (V2)-effective strain inside ASB.

to re-build the field variables. Meshfree methods have been successfully implemented in simulating crack growth phenomena. Belytschko and his co-workers have systematically applied Element Free Galerkin (EFG) method [Belytschko and Tabbara (1997)] to simulate crack growth. Liu et al [Liu et al (1999)] demonstrated

the ability of RPKM for large deformation fracture and damage problems. Li and Simonsen [Li and Simonsen (2005)] proposed the parametric visibility condition algorithm to update meshfree integration field to automatically represent the evolving crack inside a solid. Based on this algorithm, Simkins and Li [Simkins and Li (2006)] considered the thermal effect during ductile failure process, which captures some essential characteristics of ductile failure. Ren and Li [Ren and Li (2010)] proposed an automatic crack nucleation, propagation and arrest algorithm to simulate a double-crack plugging fracture process.

4.2 Parametric visibility condition algorithm

Due to the appearance of crack, the influence domains of particles nearby the crack surfaces have to be re-constructed with updated interpolation function. In Fig. 5, the dashed circle C1 and C2 denote interpolation area of two particles respectively. With the enforced visibility condition, the crack surface is treated as an opaque wall. Therefore, a particle at one side of the wall cannot 'see' the particles at the other side of the wall, which means the connection between these two particles is cut. Since crack growth is incremental, we only update the connectivity map of limited number of particles, which are located inside union of C1 (interpolation area of old crack tip) and C2 (interpolation area of current crack tip).
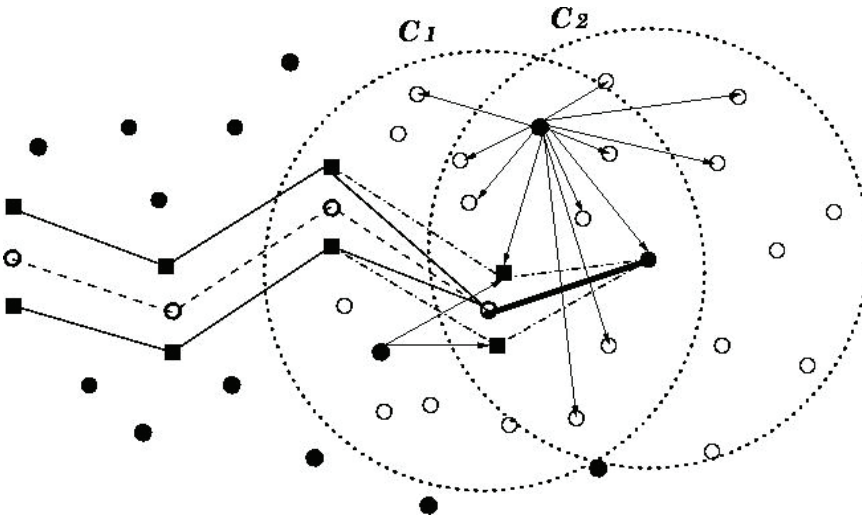

Figure 5: Modified meshfree interpolation field in front of a propagation crack tip [Li and Simonsen (2005)].

Suppose that there is a connectivity between two particles (X_{11}, Y_{11}) and (X_{12}, Y_{12}).

A line segment between old and current crack tip is located between the points (X_{21}, Y_{21}) and (X_{22}, Y_{22}) (Fig. 6). The parametric equations of these two lines are [Li and Simonsen (2005)]:

$$\begin{cases} X = X_{11} + \lambda_1 (X_{12} - X_{11}) \\ Y = Y_{11} + \lambda_1 (Y_{12} - Y_{11}) \end{cases} \tag{22}$$

$$\begin{cases} X = X_{21} + \lambda_2 (X_{22} - X_{21}) \\ Y = Y_{21} + \lambda_2 (Y_{22} - Y_{21}) \end{cases} \tag{23}$$

where λ_1 and λ_2 are the parametric variables for line segment respectively. If these two line segments intercept each other, the following parametric visibility conditions have to be satisfied (see Figure 6):

$$0 < \lambda_1 < 1 \text{ and } 0 < \lambda_2 < 1 \tag{24}$$
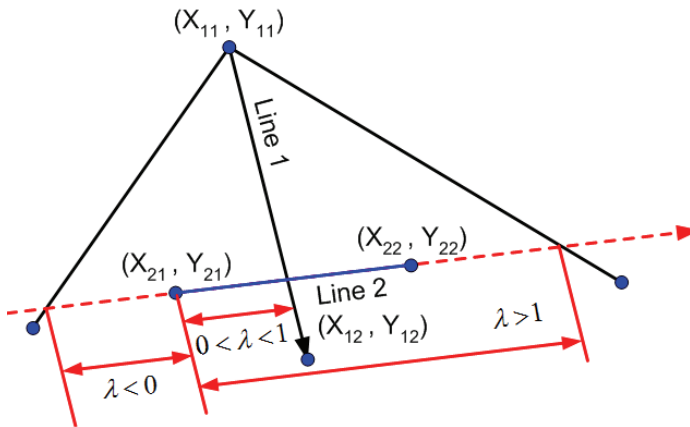
Figure 6: The illustration of the 2D parametric visibility condition.

For more detailed information of parametric visible condition, readers may refer to the references [Li and Simonsen (2005); Simkins and Li (2006)]. A sample of interpolation evolution proposed in Ren and Li [Ren and Li (2010)] is shown in Figure 7. Here the original shape function of one particle is shown as a single 'hill' (Fig. 7 (a)). After crack passes through it, its shape function will be split into two parts (Fig. 7 (b)). To visualize the morphology of evolving crack, the background mesh is also shown in Fig. 7.
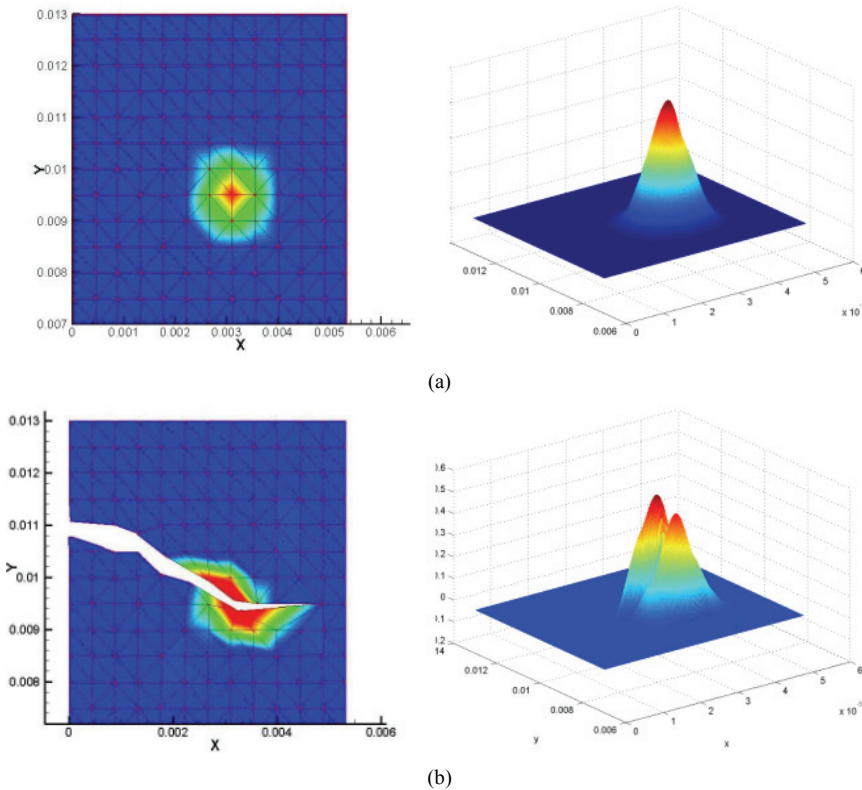
(a)

(b)

Figure 7: Meshfree shape function evolution along crack propagation: (a) Original shape function; (b) Updated shape function after crack propagation.

5 The Johnson-Cook model

The linear elastic fracture mechanics, such as those based on J-integral (Rice [1968]), requires information over a finite area to determine the fracture strength of the crack-tip. On the other hand, for inelastic fracture with large scale plastic yielding, J-integral based approach may not be justified. In this work, a damage mechanics approach with a local fracture criterion is adopted, which uses damage nucleation and growth at a single point to measure ductile failure. In this work, we use the Johnson-Cook damage model to demonstrate how the procedure works, in which the material damage at each material point is calculated according to the following

cumulative damage law ([Johnson and Cook [1985]),

$$D = \sum \frac{\Delta \varepsilon}{\varepsilon_f} \tag{25}$$

where D is the damage value, $\Delta \varepsilon$ is the plastic strain increment in one time step [Simkins and Li (2006)],

$$\varepsilon_f = \left[D_1 + D_2 \exp(D_3 \frac{\tau_m}{\bar{\tau}_y}) \right] [1 + D_4 \ln \dot{\varepsilon}] [1 + D_5 \Gamma] \tag{26}$$

$$\Gamma = \frac{T - T_{room}}{T_{melt} - T_{room}} \tag{27}$$

$\tau_m = (\tau_{11} + \tau_{22} + \tau_{33})/3$, D_1, D_2, D_3, D_4 and D_5 are material damage constants.

5.1 *Numerical results*

5.2 *crack propagation*

During the simulation, the visibility criterion is applied to all surfaces of the notches and cracks to modify the connectivities among particles. Once a crack starts to propagate, the influence domains of particles around crack surfaces will be updated and their shape functions have to be re-calculated. To illustrate the capability in handling with multiple cracks, tests are implemented on one 0.1×0.1 m plate with four horizontal notches as shown in Fig. 8(a), or two inclined notches as shown in Fig. 8(b), respectively. Velocity boundary conditions of 20 m/s are applied on both top and bottom edges to reach tension state in the plate. In addition, the Johnson-Cook model is employed with all material constants listed in Table 1. The damage contours after crack propagations for different types of notches can be found in Fig. 8.

5.3 *Crack bifurcation*

A similar procedure is applied to model crack bifurcation. As shown in Fig. 9(a), three particles around the existing crack tip will be considered as new crack tips because their damage values exceed the damage limit. Since multiple new tips are allowed, the bifurcation of crack may appear. To model such bifurcation properly, we consider the following procedure for two-dimensional cracks. Assume that there are n particles in front of the current crack tip have exceeded the damage tolerance, and then the current crack tip will be separated into the n+1 particle and n new cracks will be formed, where n is the number of simultaneous new crack
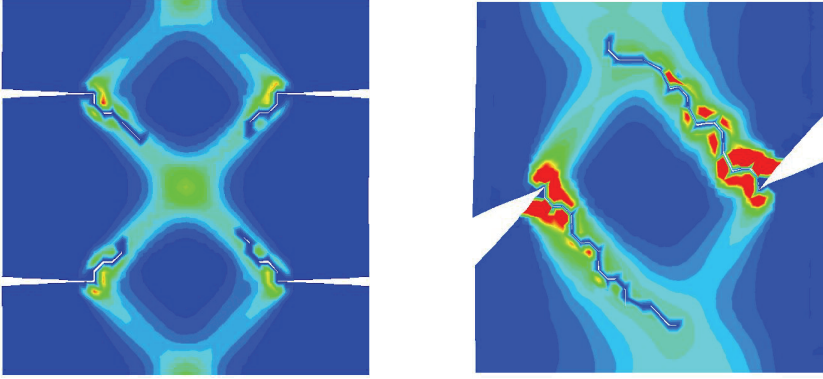
Figure 8: Damage contour after crack propagation.

tips. The field variables of all new particles, which are split from the current crack, are assigned according to the following rules,

$$
\begin{cases}
Mass_{newi} = \frac{1}{n+1}Mass_{old} \\
Volume_{newi} = \frac{1}{n+1}Volume_{old} \\
Disp_{newi} = Disp_{old} + \delta_i \\
Vel_{newi} = Vel_{old} \\
Acc_{newi} = 0.0 \\
Temp_{newi} = Temp_{old} \\
Damage_{newi} = Damage_{old}
\end{cases} \tag{28}
$$

Each branch starts the new crack propagation and the old crack tip stops growing as shown in Fig. 9(b). Then, the connectivity maps of all particles are updated according to all new crack surfaces.

To illustrate the crack bifurcation simulation, an example of tensioned-plate with a horizontal notch is considered. The plate has same material and boundary conditions as above examples except for the reduced damage tolerance value. In this example, the damage limit is reduced 30% percent to allow possible multiple new crack tips form simultaneously, which then that lead to the crack bifurcation. Fig. 10 demonstrates a bifurcation with two branching cracks.

5.4 Plugging fracture

Ren and Li [Ren and Li (2010)] simulated a plugging fracture process for a projectile impact problem, and compared with experiments. In this paper, the Kalthoff-
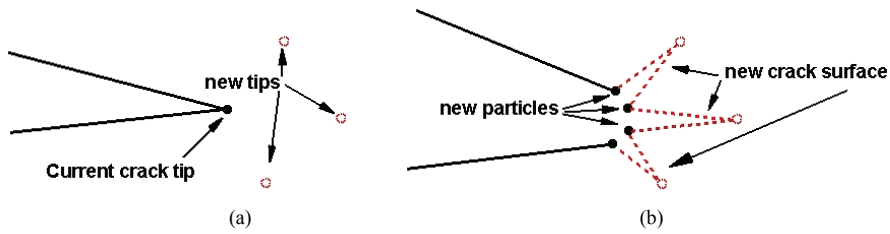
Figure 9: Sketch of forming crack branches: (a) multiple new crack tips are found nearby the existing crack tip; (b) crack branches are formed by add new particles.
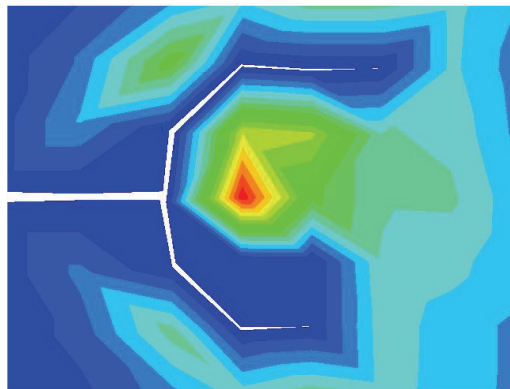

Figure 10: Crack bifurcation.

Winkler (KW) problem [Kalthoff (1988)], which is a vintage experiment set-up for ASB study, is simulated. The specimen configuration is similar as in Fig. 1, except there are two pre-set notches with a gap of 50 mm. The material constants of the specimen are list in Table 1. The damage constants are shown in Table 4. The projectile speed is 180 m/s, which is much higher than the experimental ASB speed to make crack propagation inside a specimen.

Table 4: Constants in Johnson-Cook damage model.

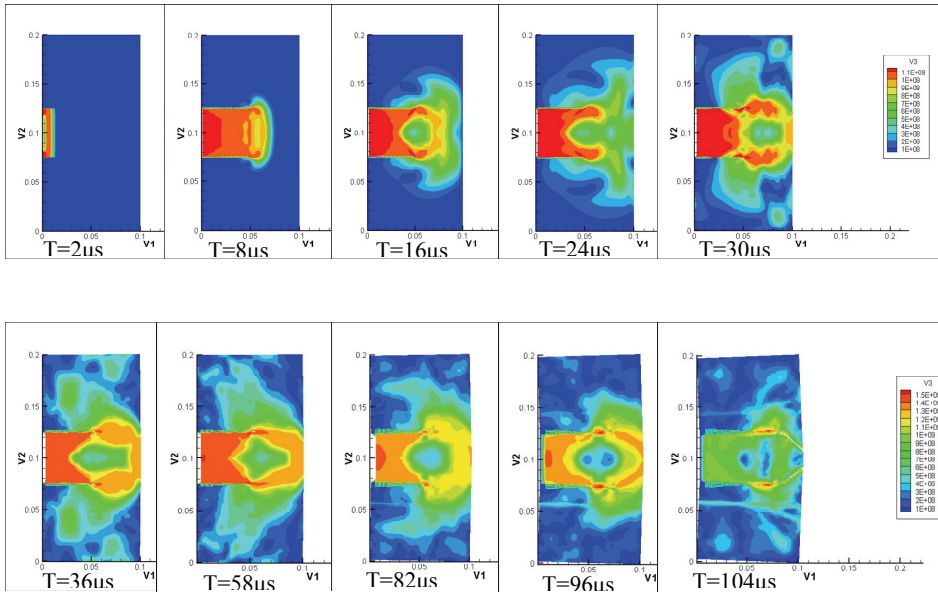| Parameter	Value	Parameter	Value
D_1	0.05	D_2	3.44
D_3	-2.12	D_4	0.002
D_5	0.61	D_{cr}	0.02

Figure 11: Time sequence of crack propagation (effective stress contour).

A time sequence of crack propagation is displayed in Fig. 11. The final crack morphology is shown in Fig 12(a). This simulation reveals some essential features of ductile failure. First, it can be seen that the high effective stress is released from the crack surface. Second, the ductile crack surface shows a zig-zag pattern, which is the essential feature of a ductile failure [Li and Simonsen (2005)]. A comparison of the ASB simulation with the crack propagation simulation in the same KW experimental set-up (projectile velocity: 80m/s) is shown in Figure 12. It can be seen that the orientation of ASB and crack path is similar, which implies that the ASB and crack interact each other during the ductile failure process.

6 Meshfree simulation of spall fracture

6.1 Overview

The ductile failure begins with nucleation of voids, which depend on the micro-scale (0.1 to 10 μm) structures of a material such as crystal grains, heterogeneous impurities and material defects [Antoun et al. (2003)]. Along with voids matrix debonding, there are ASB joining that leads to voids coalescence. This is the so-called spall fracture [Chevrier and Klepaczko (1999); Kanel (2010)]. Based on existing experimental data, a recent survey by Kanel [Kanel (2010)] discussed the
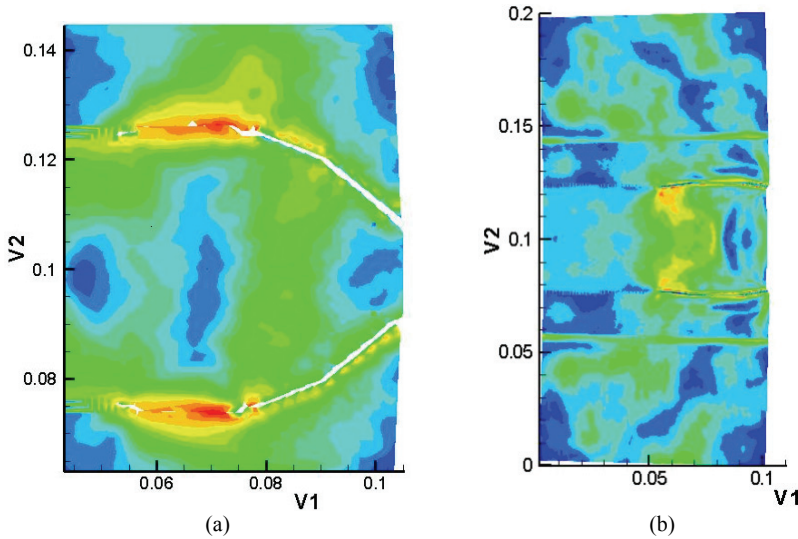
Figure 12: The ductile failure morphologies of KW problem: (a) Detailed crack surface morphology and (b) Double shear band paths.

spall fracture mechanisms and governing factors. So far, all the experiments interpret spall process by an indirect way [Chevrier and Klepaczko (1999)] from the surface velocity history. To study such dynamic spall process, numerical methods become important approaches to investigate spall phenomena. A well-known numerical model of spall fracture is void Nucleation-and-Growth method. Recently, Wright and Ramesh [Wright and Ramesh (2008)] presented a framework for a self-consistent theory of spall fracture in ductile materials. Clayton et al. [Clayton (2005); Vogler and Clayton (1993)] used a rate-dependent crystal plasticity model to simulate dynamic fracture along the grain boundaries of polycrystalline solids by cohesive finite element method. Ren et al [Ren et al (2011)] related the macro-scale spall strength to the kinematics of micro void growth in a Representative Volume Element (RVE), and proposed a meshfree algorithm of void nucleation, growth and coalescence.

6.2   *The multi-scale spall strength formulas*

Experimental studies illustrate that spall strength (the tensile stress just before the spall fracture nucleation) is related to the duration of loading, i.e., the rate of volume deformation. Based on the experimental data, Antoun et al [Antoun et al (2003)] formulated a well-validated empirical equation to calculate the spall strength of

solid, which is given as follow,

$$\sigma^{spall} = A \left(\frac{\dot{V}}{V_0} \right)^m \tag{29}$$

where A and *m* are material constants. The symbol V denotes the total volume of material at current time and V_0 is the total volume of material at initial configuration. The empirical spall strength is a function of macro-scale properties of a solid, based on a quasi-static theory. The macro-scale mechanics variables can be defined as the average value of a microscopic element. A solid with internal voids can be considered as a porous material, and its overall mechanical responses may be modeled by using the Representative Volume Element (RVE) with an outer surface that encloses a fixed mass and certain number of voids (Figure 13). Assume that the center of the RVE is located at $\bar{x}(t)$.
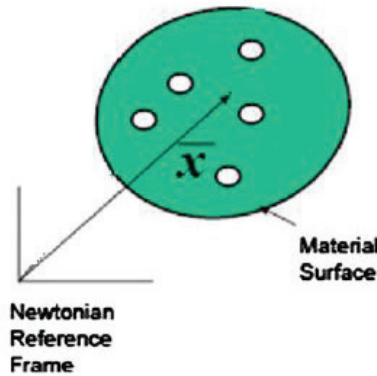

Figure 13: Representation Volume Element (RVE) with spall voids inside material.

Considering a porous material, the total volume of material can be divided into two parts: V_s (volume of solid) and V_υ (volume of voids). If the material is incompressible, from the definition of RVE, we have

$$\dot{V} = \dot{V}_s + \dot{V}_\upsilon \tag{30}$$

Assume that initially that the material has no defects, which means that $V_0=V_s$ at t = 0. Then the empirical spall strength formula can be written as

$$\sigma^{spall} = A \left(\frac{\dot{V}_\upsilon}{V_s} \right)^m \tag{31}$$

Let f be the void volume per unit total volume, i.e., the void fraction in porous material

$$f = \frac{V_v}{V} \tag{32}$$

The rate of void growth $\dot{f}$ can be defined as

$$\dot{f} == \frac{\dot{V}_v}{V_s}(1-f)^2 \tag{33}$$

Then we can connect the spall strength to micro scale quantities f and $\dot{f}$ as follows

$$\sigma^{spall} = A\left(\frac{\dot{f}}{(1-f)^2}\right)^m \tag{34}$$

Following Wright and Ramesh [Wright and Ramesh (2008)], $\dot{f}$ can be defined as

$$\dot{f} = 1 - f\left(\dot{\bar{x}}_{i,i} - \frac{\dot{\bar{p}}}{\bar{k}(f)}\right) \tag{35}$$

$$\bar{k}(f) = k\frac{4(1-f)\mu}{4\mu + 3fk} \tag{36}$$

where $\dot{p}$ is spherical stress rate, k is bulk modulus and μ is the shear modulus. It is speculated that a spall fracture is induced by the tri-axial tensile stress. In this paper, we use the spherical stress of the second Piola-Kirchhoff stress (PK-II) p as the control variable in the spall fracture criterion of a meshfree particle. And, two spall fracture criteria are employed: 1) the spall strength exceeds the critical value, and 2) the spherical stress p exceeds its spall strength:

$$\sigma^{spall} \geq \sigma_{cr} \text{ and } p \geq \sigma^{spall} \tag{37}$$

6.3 Numerical simulations

In this simulation, a target-flyer impact simulation has been carried out to study the dynamic spall fracture process. The flyer impacts one side of specimen with a velocity of 100 m/s. The flyer is modeled as a rigid plate and the dimension of the target plate is 2 mm x 10 mm. The material properties of the target plate are modeled by the Johnson-Cook model with material constants shown in Table 5 and Table 6.

The dynamic evolution of spherical stress is shown in Fig. 14. Since spherical stress provides direct evidence of the presence of shock wave, we actually find that it is

Table 5: Johnson-Cook material constants for the target plate.

Parameter	Value	Definition
E	200GPa	Young's modulus
v	0.3	Poisson's ratio
ρ	7850 kgm^{-3}	Mass density
A	490MPa	Yield stress
B	807MPa	Strain Hardening
n	0.73	Strain hardening index
$\dot{\varepsilon}_0$	1.0s^{-1}	Reference strain rate
m	0.94	Temperature softening
C_p	452J(Kg.K)$^{-1}$	Specific heat
α	11.2E-06K^{-1}	Coefficient of Thermal expansion
χ	0.9	The fraction of plastic work convert to heat
k	38	Conductivity coefficient

Table 6: Spall fracture criterion constants for the target plate.

Parameter	Value	Definition
A	0.65GPa	Empirical constant
m	0.11	Empirical constant
σ_{cr}	2.5e8	The minimum of spall strength for voids nucleation
p_{cr}	2.0e9	The critical value for void growth

the tensile spherical stress wave that drives the spall nucleation and growth. Spall voids nucleate at the twinkle when the high tensile spherical stress (orange to red region) is reached. After that moment, the stress wave propagation is disturbed by the newly formed voids. When the tensile spherical stress wave comes back to existing spall voids, these voids keep growing and coalesce each other. From the final morphology of spall fracture, Fig. 15, we can find the fracture zone is distributed inside the specimen with large plastic strain, and more spall voids are nucleated near the ends of vertical spall fracture zone, which is caused by the boundary effect of the specimen, which was not observed in the previous work [Ren et al (2011)].

7   Discussions and conclusions

The ductile failure is characterized with numerous plastic deformations. It is a complex multi-physics and multi-scale process that evolves from micro-scale voids to macro-scale crack propagation. The development of experimental method, damage
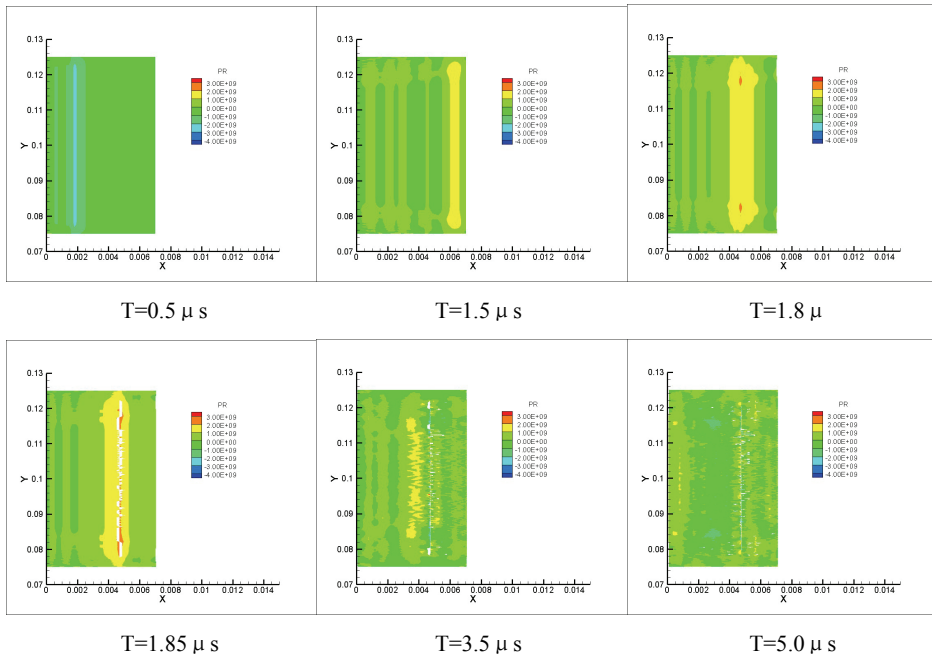
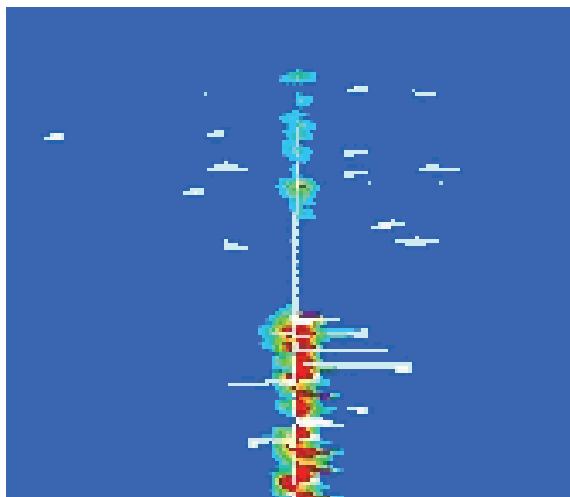Figure 14: Time sequence of spall fracture (Color contour is spherical stress).

Figure 15: Spall fracture morphology shown as plastic strain.

mechanism, and numerical modeling theory for ductile failure is still under active investigations.

From the numerical point of view, the simulation of a dynamic fracture process means evolution of the computational domain. Meshfree has intrinsic advantages in simulating this kind of problems. This paper reviewed the current state-of-the-art numerical simulation theories of three main ductile failure phenomenas. A mesh-free formula with thermo-mechanical coupling and Johnson-cook model are proposed. For ASB simulation, based on a multi-physical method, an application of the Zhou-Rosakis-Ravichandran (ZRR) problem is reported. The stress collapse and thermal effect inside shear band are discussed. We found that the average velocity of ASB is 1100 m/s and the maximum temperature inside shear band is 1266 K, which is consistent with the experimental results reported by Zhou et al. (1996a). For macro-crack simulation, the Parametric Visibility Condition algorithm is discussed and a double crack Kalthoff-Winkler (KW) problem is simulated. The final fracture morphology shows ASB and crack interact with each other in ductile failure. For spall fracture, we calculate the macro-scale spall strength from the micro-scale features of voids and capture the dynamic spall fracture process. The numerical simulations demonstrate that meshfree method can capture the main essential features of a ductile failure.

References

Antoun, T.; Seaman, L.; Curran, D.R.; Kane, G.I.; Razoreno, S. V.; Utkin, A.V. (2003): Spall Fracture, Springer, New York.

Armero, F.; Simo, J. C. (1993): A priori stability estimate and unconditionally stable product formula algorithm for nonlinear coupled thermo plasticity, *International Journal of Plastic*ity, vol. 9, 749-782.

Chevrier, P.; Klepaczko, J. R. (1999): Spall fracture: Mechanical and microstructural aspects, *Engineering Fracture Mechanics*, vol. 63, 273-294.

Atluri, S. N.; Zhu, T. (1998): A new Meshless Local Petrov-Galerkin (MLPG) approach in computational mechanics, Computational Mechanics, vol. 22, 117-127.

Atluri, S. N.; Zhu, T. (2000): The meshless local Petrov-Galerkin (MLPG) approach for solving problems in elasto-statics, vol. 25, 169-179.

Bai, Y.; Dodd, B. (1992): Adiabatic Shear Band Localization, Pergamon Press, New York.

Batra, R.C.; Kim, C.H. (1992): Analysis of shear banding in twelve materials, *Int. J. Plasticity,* vol. 8, 425–452.

Belytschko, T.; Tabbara, M. (1997): Dynamic fracture using element-free Galerkin methods, *Journal of Computational and Applied Mathematics*, vol. 39, 923–938.

Chevrier, P.; Klepaczko, J.R. (1999): Spall fracture: Mechanical and microstructural aspects, *Engineering Fracture Mechanics*, vol. 63, 273-294.

Clayton, J.D. (2005): Modeling dynamic plasticity and spall fracture in high density polycrystalline alloys, *International Journal of Solids and Structures*, vol. 42, 4613-4640.

Johnson, G.R.; Cook, W.H. (1985): Fracture characteristics of three metals subjected to various strains, Strain Rates, Temperatures and Pressures, *Engineering Fracture mechanics*, vol. 21, 31-48.

Kalthoff, J.F. (1988): Shadow optical analysis of dynamic shear fracture, *Optical Engineering*, vol. 27(10), 835-840.

Kanel, G.I. (2010): Spall Fracture: methodological aspects, mechanisms and governing factors, *International Journal of Fracture*, vol. 163, 173-191.

Li, S.; Hao, W.; Liu, W. K. (2000): Mesh-free simulations of shear banding in large deformation, *International Journal of Solids and Structures*, vol. 37, 7185-7206.

Li, S.; Liu, W. K. (2000): Numerical simulations of strain localization in inelastic solids using mesh-free methods, *International Journal.for Numeical. Methods in Engineering*, vol. 48, 1285-1309.

Li, S; Liu, W.K. (2002): Meshfree and particle methods and their applications, *Applied Mechnics Review*, vol. 55(1), 1-34.

Li, S.; Liu, W.K. (2004): Meshfree Particle Method, Springer-Verlag, Berlin, Germany.

Li, S.; Liu, W.K.; Qian, D.; Guduru, P. R.; Rosakis, A. J. (2001): Dynamic shear band propagation and micrco-structure of adiabatic shear band, *Comput. methods appl. mech. engrg*, vol. 191, 73-92.

Li, S.; Liu, W. K.; Rosakis, A. J.; Belytschko, T.; Hao, W. (2002): Mesh-free Galerkin simulations of dynamic shear band propagation and failure mode transition, *International Journal of Solids and Structures*, vol. 39, 1213–1240.

Li, S.; Simonsen, C. B. (2005): Meshfree simulations of ductile crack propagations, *International Journal for Computational Methods in Engineering Science*

and Mechanics, vol. 6, 1–19.

Liu, W. K.; Hao, S., Belytschko, T.; Li, S., Chang, C. T. (1999): Multiple scale meshfree methods for damage fracture and localization, *Computational Materials Science*, vol. 16, 197-205.

McVeigh, C.; Liu, W.K. (2009): Multiresolution modeling of ductile reinforced brittle composites, *J. Mech. Phys. Solids*, vol. 57, 244-267.

Medyanik,S. N.; Liu, W. K.; Li, S. (2007): On criteria for dynamic adiabatic shear band propagation, *Journal of the Mechanics and Physics of Solids*, vol. 55, 1439–1461.

Nahshon, K.; Hutchinson, J.W. (2008): Modification of the Gurson Model for shear failure, *European Journal of Mechanics A/Solids*, vol. 27, 1-17.

Rice, J.R. (1968), A path independent integral and the approximate analysis of strain concentration by notches and cracks, ASME, Journal of Applied Mechanics, **35**, 379-386.

Ren, B.; Li, S. (2010): Meshfree simulations of plugging failures in high-speed impacts, *Computers and Structures*, vol. 88, 909-923.

Ren, B.; Li, S.; Qian, J.; Zeng, X. (2011): Meshfree simulations of spall fracture, *Computer Methods in Applied Mechanics and Engineering*, vol. 200, 797-811.

Simkins, D. C.; Li, S. (2006): Meshfree simulations of thermo-mechanical ductile fracture. *Comput. Mech*, vol. 38, 235–249.

Vogler, T.J.; Clayton, J.D. (1993): Heterogeneous deformation and spall of an extruded tungsten alloy: plate impact experiments and crystal plasticity modeling, *Journal of the mechanics and physics of solids*, vol. 9, 297-335.

Wright, T.W.; Ramesh, K.T. (2008): Dynamic void nucleation and growth in solids: A self-consistent statistical theory, *Journal of the mechanics and physics of solids*, vol. 9, 297-335.

Zhou, M.; Rosakis, A. J.; Ravichandran, G. (1996a): Dynamically Propagating Shear Bands in Impact-loaded Prenotched Plates - I. Experimental investigations of temperature signatures and propagation speed, *Journal of Mechanics of Physics and Solids*, vol. 44, 981-1006.

Zhou, M.; Ravichandran, G.; Rosakis, A. J. (1996b): Dynamically propagating shear bands in impact-loaded prenotched plates - II. Numerical Simulations, *Journal of Mechanics of Physics and Solids*, vol. 44, 1007-1032.

CMES: Computer Modeling in Engineering & Sciences